Cryogenic Deformation Behaviour of Aluminium Alloy 6061-T6

Minsoo Jin[1] · Byungju Lee[1] · Jisung Yoo[1] · Yonghee Jo[2] · Seunggun Lee[1]

Abstract

Aluminium alloy 6061-T6 (AA6061-T6) shows a promising potential for cryogenic structural applications. This alloy exhibits remarkable monotonic tensile properties at low temperatures. However, there is a limited number of studies on the cryogenic deformation behaviour. In this study, both monotonic and cyclic loading were conducted, and various microstructure characterisation techniques were performed to understand influence of cryogenic temperatures on microstructure evolution and deformation behaviour of this alloy. At cryogenic temperatures, the aluminium alloy exhibited superior mechanical properties over those at room temperature. Yield stress, UTS and elongation at failure increased by 18%, 33%, and 53% at 77 K compared to those at room temperature. Such increase in mechanical properties was attributed by the stronger resistance to dislocation movement due to the reduced thermal assistance. Work hardening rate also increased as dynamic recovery was suppressed at lower temperatures. As a result, a high density of dislocations was evenly distributed within grain interior and led to a homogeneous deformation. The test temperature appeared to have a significant influence on fatigue performance; maximum stress response increased by 23% at 108 K with respect to those at room temperature. During cyclic loading, a high number of dislocations was generated to accommodate prescribed strain because of the resistance to dislocation movement including the pinning of dislocations by β'' precipitates which are known to be sheared at room temperature. Thus, the alloy exhibited an enhanced cyclic hardening behaviour without a noticeable cyclic softening phase. Fatigue life improved by 143% at 108 K with respect to that at room temperature as the homogeneous deformation prohibited localised slip activity and delayed formation of slip bands which act as crack initiation sites. Moreover, the initiation and propagation of secondary cracks at 108 K retarded the propagation of main crack to improve fatigue life.

Keywords Al–Mg–Si alloy · Cryogenic · Mechanical properties · Fatigue · Low temperature

1 Introduction

In the recent decade, the replacement of carbon-based fossil fuels has been a crucial issue considering the serious climate change crisis. In order to overcome the crisis, hydrogen has been recognised as a sustainable alternative energy source thanks to its abundant availability and zero emission characteristic [1, 2]. In particular, liquid hydrogen has been considered as it exhibits a high transportation efficiency owing to a high storage density. Importantly, liquid hydrogen can be stored at an atmospheric pressure, which allows to maintain a higher degree of safety in comparison to the gaseous hydrogen stored at a high-pressure [3]. Hydrogen liquefies at an extremely low temperature of 20 K, and application of alloy components at cryogenic conditions poses a challenge in material selection. The material should be able to withstand extremely low temperatures without embrittlement while maintaining good strength and fracture toughness.

For cryogenic applications, aluminium alloys have received a significant interest as a potential candidate owing to their good strength-to-weight ratio. In the recent decades, an extensive number of studies have reported that aluminium alloys exhibit enhanced tensile properties at cryogenic temperatures [4–13]. Furthermore, aluminium alloys have been

Minsoo Jin, Byungju Lee and Jisung Yoo have contributed equally to this work.

✉ Seunggun Lee
jmins94@kims.re.kr

1   Department of Hydrogen Materials Evaluation, Extreme Materials Institute, Korea Institute of Materials Science, Changwon 51508, Republic of Korea

2   Department of Aluminium, Advanced Metals Division, Korea Institute of Materials Science, Changwon 51508, Republic of Korea

utilized for the cryogenic structural application such tanks for liquefied natural gas (LNG) at 108 K [4–8]. Among various aluminium alloys, AA6061-T6 is a precipitation hardening alloy with a combination of good mechanical properties, weldability, and formability [9, 14, 15]. The study by Park et al. [8] showed that there was a significant increase in tensile properties of AA 6061-T6 with decreasing temperatures; yield stress and ultimate tensile strength (UTS) increased by 16% and 20% at 110 K, respectively, compared to those at room temperature. Magalhães et al. [16] also reported strong temperature dependent mechanical properties of the AA 6061 (with no T6 artificial ageing). UTS increased by 56% at 77 K in comparison to that at room temperature, and the elongation at fracture increased from 30 to 47% as temperature decreased to 77 K. Such fascinating low temperature mechanical properties indicate this alloy holds a promising potential as a reliable structural alloy at cryogenic conditions.

Despite the remarkable cryogenic tensile properties, there is a limited number of studies is available on the cryogenic deformation behaviour of this alloy [8, 9, 16]. Understanding cryogenic deformation behaviour especially fatigue behaviour is important as most of mechanical systems operate under cyclic loading conditions, and most of the failures of the systems were associated with cyclic plasticity and fatigue damage [17–19]. This suggests a need for the study focusing on the cryogenic deformation behaviour and fatigue properties of this alloy. There are some preceding studies on cryogenic fatigue behaviour of aluminium alloys with different chemical compositions (e.g., AA5083 and Al–Li alloys) are available [20–23]. These studies on AA5083 and Al–Li alloys [21–23] mainly focused on the investigation of fracture surfaces to analyse fracture mechanisms after cryogenic fatigue test, except for the research of Xu et al. [20] which represented a detailed observation on microstructure evolution in Al–Li alloy (Al 8090-T6). The author reported that the decrease of test temperature increases the fatigue strength by changing the deformation mode. The fracture at liquid nitrogen temperature exhibited deeper and larger numbers of delaminations which seem to disperse the strain concentration, leading to the shear deformation localisation. The dislocation behaviour changed from inhomogeneous planar slip to homogeneous distribution in grains with decreasing temperature, contributing to the improved fatigue performances at cryogenic temperatures. However, to the author's knowledge, the study concerning the fatigue properties of the current AA6061-T6 under cryogenic conditions is very limited. Especially, investigation on cyclic plasticity (i.e., cyclic softening and hardening) in terms of microstructures including crystallographic analysis and the dislocation behaviour in precipitation hardened AA6061-T6 alloy at cryogenic conditions is still lacking. Therefore, the aim of this study is to provide an in-depth understanding on microstructure evolution and both monotonic and cyclic deformation behaviour at cryogenic temperatures to recognise the potential of the aluminium alloy. The current study was conducted at two well-known cryogenic conditions, liquefied natural gas (108 K) and liquid nitrogen (77 K) temperatures, prior at the liquid hydrogen temperature (20 K). However, as mentioned in the first paragraph, the authors are also aware of the significance of liquid hydrogen. Hence, a subsequent study is currently in progress investigating the mechanical performances and microstructural evolution of the current alloy at 20 K. Ultimately, the collection experimental results of the current study and the following study can establish a database of the current alloy, verifying its reliability over a wide range of cryogenic temperatures.

2 Experimental

2.1 Materials and Heat Treatment Process

The material used for this study was a commercial aluminium alloy 6061 (Al–Mg–Si) sheet with a thickness of 15 mm. The chemical composition (wt%) of the aluminium alloy is given in Table 1. The aluminium sheet was heat treated according to T6 Temper process presented in Fig. 1. The aluminium sheet was solution treated at 793 K (520 °C) for 1 h followed by water quenching, then artificially aged at 453 K (180 °C) for 8 h and air cooled.

2.2 Microstructure characterisation

Fractography of tensile tested and fatigued specimens were carried using JEOL 7100F scanning electron microscope (SEM). For EBSD analysis, the tensile tested specimens were cut along their longitudinal axis, which corresponds to the loading direction. Phases of AA6061-T6 were identified using X-ray diffraction analysis (XRD, D/Max-2500, Rigaku Co., USA, radiation Cu Kα, wavelength 1.5406 Å, scan rate 5° min^{-1}). The specimens ground using silica grit papers (500, 1200, 2400, 4000), and polished in an OP-S solution with 0.4 for electron backscattered diffraction (EBSD) analysis. EBSD analyses were performed using a Hitachi SU-6600 SEM equipped with a Field Emission Gun (FEG) electron source and a voltage of 20 kV. EBSD analyses were set at a step size of 0.3 µm per pixel and grain boundaries were defined at a misorientation larger than 5°. Discs with a diameter of 3 mm were prepared from the gauge parts of the fatigued specimens. The discs were electrochemically polished at 30 V and − 30 °C using a twin-jet Struers Tenupol in an electrolyte consisting of 30% nitric acid in methanol for transmission electron microscopy (TEM) investigation. Bright field (BF) TEM analysis was conducted using JEOL 2100F at voltages of 100 eV and 200 eV.

2.3 Mechanical Testing

Cylindrical dog bone specimens were prepared from the as-received AA6061-T6 sheet with for tensile tests in accordance with ASTM E8 standard (gauge length of 25 mm, parallel to rolling direction). Tensile tests were performed at three different temperatures (room temperature (RT), 108 K and 77 K) with a strain rate of 10^{-4} s^{-1}. The tensile tests were conducted three times at each temperature condition. Strain-controlled fatigue tests were conducted at a strain amplitude of $+0.5\%$ (R = 0.01, 0.1 Hz). The fatigue tests were conducted at two different temperature conditions: room temperature (RT) and 108 K. The lowest temperature that could be during fatigue test was 108 K due to limitations in test machine specifications, and 108 K was maintained by controlling input amount of liquid nitrogen into chamber. Fatigue life was defined at a number of cycles when maximum stress response dropped by 20% from a plateau region.

3 Results

3.1 Microstructural Characterization and Mechanical Properties

Figure 2 shows as-received microstructure of aluminium alloy 6061-T6 (Fig. 2). EBSD IPF and IQ map show grains on normal direction (ND) plane are elongated towards rolling direction (RD), and their average grain size was 310 ± 50 μm (Fig. 2a). KAM map revealed volume fraction of 48% has been recrystallised during solution treatment, but some grains remained without recrystallisation with a higher KAM value (Fig. 2b). Compressive stress during extrusion of the AA6061 sheet resulted in grains elongated along transverse direction (TD) as shown in RD plane IPF + IQ map. Their average grain size was 170 ± 34 μm with a narrower width in comparison to those on the ND plane. The volume fraction of recrystallisation was 29%. Mechanical tests were conducted with the loading axis that was parallel to the RD and gauge of specimens.

Figure 3 and Table 2 present monotonic tensile properties of AA6061-T6 at three different temperatures (RT, 108 K, and 77 K). Yield stress, ultimate tensile strength (UTS), and elongation at failure of the aluminium alloy increased significantly with decreasing temperature. The yield stress, UTS and elongation increased by 18%, 33%, and 53% at 77 K compared to those at room temperature. Figure 4 shows true stress–strain curves (solid lines) and corresponding work hardening rate curves (dashed lines) of specimens tested at the three different temperatures. The work hardening rate of the aluminium alloy increased significantly with decreasing temperature. The true strain value at the intersection between the tensile curve and the work hardening curve represents percentage of a uniform elongation [24]. The uniform elongation of the aluminium alloy increased from 9 to 12% and 14% as temperature decreased from RT to 108 K and 77 K, respectively.

Figure 5 shows the maximum stress responses of the aluminium alloy during cyclic loading at RT and 108 K. Cyclic hardening behaviour was observed regardless of test temperature. At room temperature, specimens exhibited a short cyclic hardening during the first 5 cycles, followed by cyclic softening. On the other hand, a cyclic hardening behaviour with a higher hardening rate continued up to the first 100th cycles at 108 K, followed by a constant maximum stress response up to ~700th cycle with no apparent cyclic softening stage. The test temperature appeared to have a significant influence on fatigue performance; maximum stress response increased by 23%, and fatigue life improved by 143% at 108 K with respect to those at room temperature (Table 3).

3.2 Fracture Surface Examination

Fractography of the specimens after tensile tests at the three different temperatures (RT, 108 K, 77 K) (Fig. 6) shows ductile dimples on fracture surfaces of the specimens, indicating ductile fracture occurred regardless of the test temperatures. Aluminium oxide inclusions were often observed on the fracture surface of the specimens tested at the low temperatures (108 K, 77 K) (indicated by white arrow shown in Fig. 6c and e). Nevertheless, the aluminium oxide inclusions were embedded in ductile dimple region without trace of brittle cleavage fractureThis indicates that they work as initiating sites of microvoids to form dimples on the fracture surface at cryogenic temperatures [25]. Furthermore, the improved ductility at cryogenic temperatures (Fig. 3 and Table 2) despite the presence of the aluminium oxides also suggests the influence of the oxides on fracture behaviour was insignificant.

Fractography of the specimen fatigued at room temperature show cracks initiated from the free surface of the specimen with river patterns (Fig. 7a). The crack initiation sites are indicated with yellow dashed circles, and five initiation sites were observed. The fracture surface was seen to be transgranular with fatigue striations. The striations

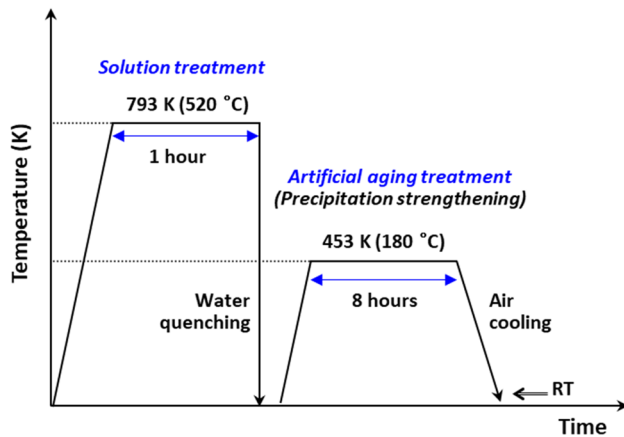| Table 1 Chemical composition of the aluminium alloy 6061-T6	Element	Al	Mg	Si	Fe	Cu	Mn	Cr	Zn	Ti
	wt%	Balance	1.02	0.5	0.33	0.21	0.085	0.14	0.009	0.013

Fig. 1 A schematic diagram of the T6 heat treatment procedure

became broader along crack propagation direction which was towards the centre of the specimen (Fig. 7b–d). Ductile dimples were found at the centre region (Fig. 7e), indicating a ductile fracture occurred due to an overload by reduction in load-bearing area with crack propagation.

Fracture surface of the specimen fatigued at 108 K appeared to be similar to that at the room temperature. Crack initiation sites with river patterns were observed at free surface of the specimen fatigued at 108 K (Fig. 8a), and fracture mode appeared to be transgranular. Aluminium oxide inclusions were not observed at crack initiation sites, suggesting their influence on fracture behaviour was negligible. Ductile dimples were also present at overloaded region (Fig. 8b). The significant difference at 108 K was presence of secondary cracks on the fracture surface, rather than the evolution of striation (indicated by blue ellipsoids shown in Fig. 8c–e). These secondary cracks were located along crack propagation direction and propagated in a direction perpendicular to the primary crack propagation direction.

3.3 Microstructure Evolution After Deformation

Figure 9 shows the microstructures of the specimen after tensile tests at room temperature and 77 K. Kernel Average Misorientation (KAM) maps show GND density varied in each grain within the same specimen. As demonstrated in Fig. 2b, d, some grains remained without recrystallisation after solution treatment (indicated by the black dashed lines shown in Fig. 9a, b). The accumulation of the GNDs generated during the rolling and the GNDs generated during tensile test resulted in a higher GND density in the non-recrystallised grains in comparison to the recrystallised grain. Hence, the line profile analysis was conducted along the recrystallised grains to analyse only the GNDs generated during tensile tests. Figure 9a shows the KAM map of the specimen tested at room temperature with the line

profile analysis across a recrystallised grain (indicated by the white dashed arrow shown in Fig. 9a). Figure 9c presents misorientation (red curve) and KAM values (blue curve) corresponding to the line profile analysis. A steep rise of the red misorientation curve was seen at grain boundaries (GBs), and blue KAM curve also reached a peak near GBs. The high KAM values at GBs is associated with the strain localisation due to dislocation pile up as GBs act as barriers to gliding dislocations [26]. The noticeable increase in dislocation density at GBs at room temperature suggest that inhomogeneous plastic deformation occurred at GBs rather than grain interior. On the other hand, the KAM map and line profile analysis of the sample tested at 77 K showed a different tendency in microstructure evolution (Fig. 9b). The line profile analysis along the grains in the sample tested at 77 K showed rises of the blue KAM curve between GBs (peaks of the red misorientation curves) (Fig. 9b), indicating there was a noticeable increase in dislocation density within interior of the grains. Dislocations were distributed homogeneously within grain interior at the cryogenic temperature in comparison to that at room temperature (Fig. 9d). Moreover, a slip trace along {111} planes (red lines shown in Fig. 9e) suggests strain localisation developed within the grain interior.

Figure 10 shows x-ray diffraction patterns of AA6061-T6 in as-received state, and after tensile tests at room temperature, 108 K and 77 K with diffraction peaks corresponding to aluminium matrix. Dislocation density (ρ) was determined from the XRD peak profiles using the Debye–Scherrer equation [27, 28]:

$$\rho = \frac{1}{D^2} \tag{1}$$

$$D = \frac{K\lambda}{\beta cos\theta} \tag{2}$$

where D is the crystal size, K is a constant (0.9) [28], and λ is the wavelength of the incident X-ray (1.5406 Å), β is the fill width at half maximum (FWHM), and θ is the Bragg angle of the major XRD peaks. The miller indices (hkl), 2-theta (2θ), FWHM, and dislocation density (ρ) along the major diffraction peaks (111) and (200) are summarised in Table 4. XRD was performed at least three times for each specimen to ensure data reproducibility. The average dislocation density for the as-received state, and after tensile tests at room temperature, 108 K and 77 K are $4.256 \pm 0.89 \times 10^{14}$, $7.698 \pm 0.57 \times 10^{14}$, $8.004 \pm 0.29 \times 10^{14}$, and $8.361 \pm 0.37 \times 10^{14}$ m^{-2}, respectively. This shows that the dislocation density increased through the applied strain during tensile test, and that the increase in elongation as the test temperature decreases can further increase the dislocation density. In the preceding study by Liu et al. [9], the
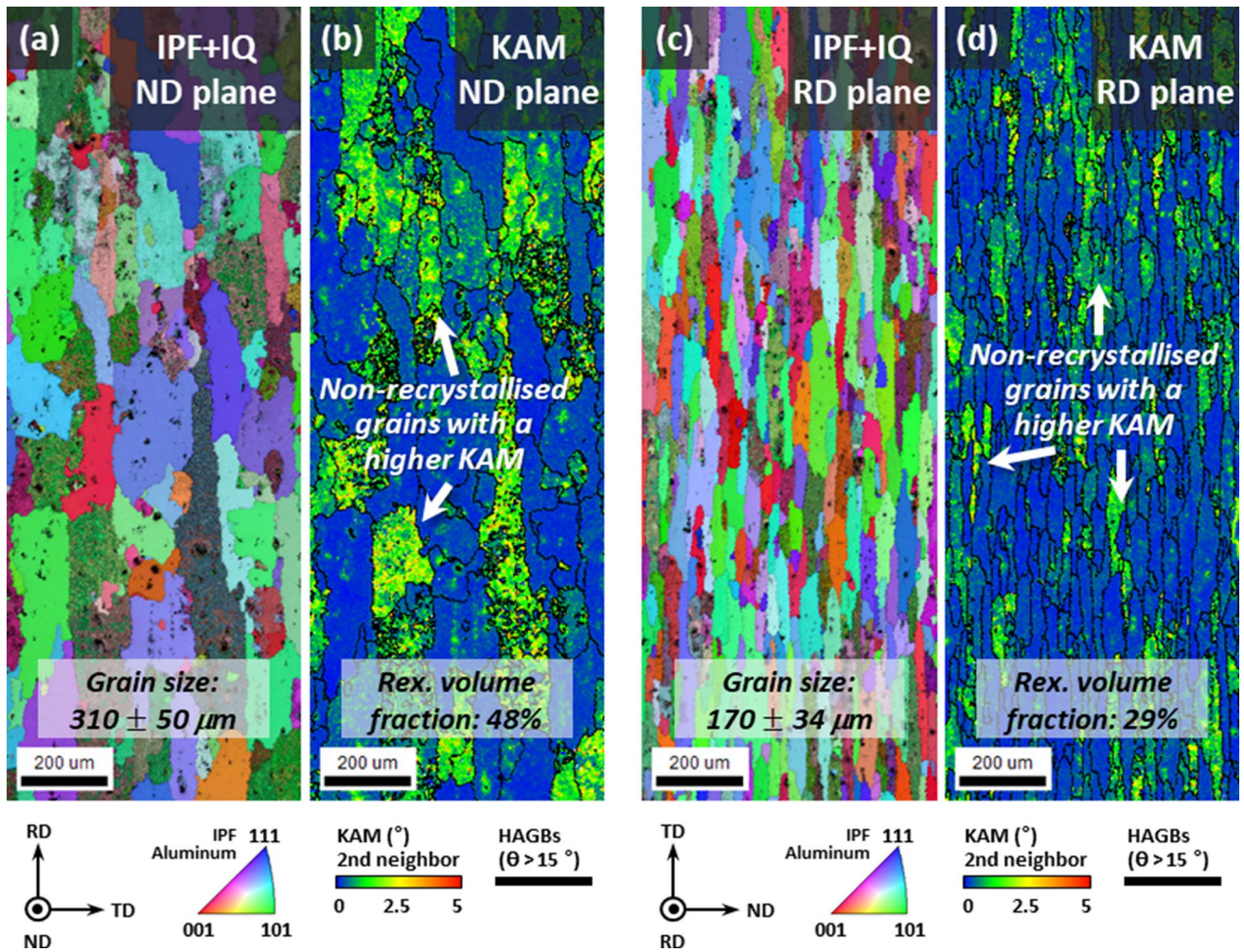
Fig. 2 As-received microstructure of AA6061-T6 specimens. **a** IPF and IQ map, and **b** KAM map with volume fraction of recrystallised grains on ND plane. **c** IPF and IQ map, and **d** KAM map with volume fraction of recrystallised grains on RD plane
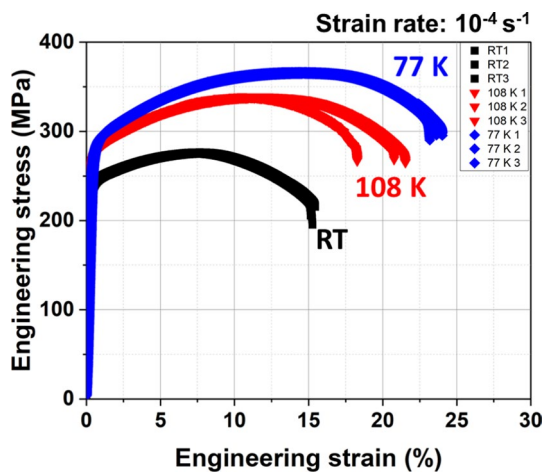

Fig. 3 Monotonic tensile stress–strain curve of aluminium alloy 6061-T6 at the three different temperatures (RT, 108 K, 77 K)

Table 2 Tensile properties of AA6061-T6 at room temperature, 108 K and 77 K

Condition	Yield stress (MPa)	Ultimate tensile stress (UTS) (MPa)	Elongation at failure (%)
RT	238 ± 2	274 ± 1	15.5 ± 0.3
108 K	268 ± 1	337 ± 1	20 ± 1.5
77 K	280 ± 2	366 ± 3	23.6 ± 0.4

dislocation density increased by about 0.58×10^{14} m^{-2} as the rolling reduction ratio increased from 50 to 70% in a solution treated 6061 alloy. In addition, in the study examining the dislocation density during tensile test of 7020-T6 alloy, the change in dislocation density according to tensile strain was about 0.6×10^{14} m^{-2}, which is similar to our observations [29]. Therefore, it is believed that our results are reliable and
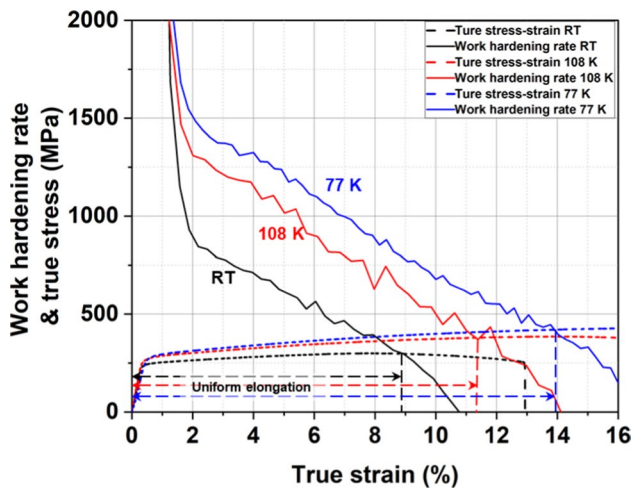
Fig. 4 True tensile stress–strain curves of AA6061-T6 (dashed lines) and work hardening rate curves (solid lines) at room temperature (RT), 108 K and 77 K
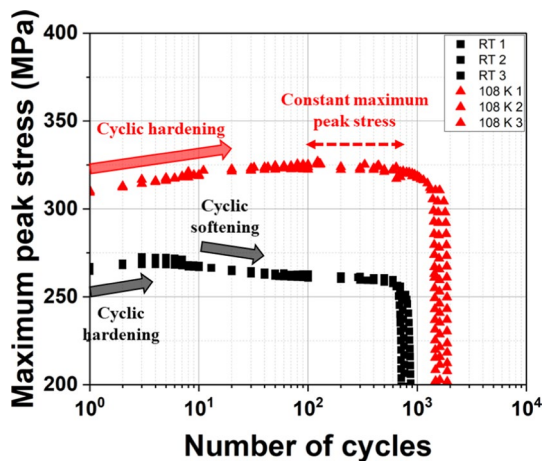

Fig. 5 Evolution of the maximum peak stresses of the AA6061-T6 specimens during cyclic loading at room temperature (RT) and 108 K

Table 3 Fatigue lives of AA6061-T6 samples at room temperature and 108 K

Condition	Number of cycles at 20% stress drop
RT_#1	760
RT_#2	730
RT_#3	820
108 K_#1	1870
108 K_#2	1930
108 K_#3	1820

there is a clear difference in dislocation densities depending on applied strain in different temperature.

Figure 11a–d are BF TEM images of dislocation structure and active dislocation glide (Fig. 11a–c) in the specimen

fatigued fractured at room temperature showing. Figure 11a shows dislocations rearranged themselves to form a dislocation wall with a thickness of ~ 0.2 μm throughout cyclic loadings. Dislocation walls were observed as the number of cycles at room temperature was too short to form cell structures. Glide of dislocations was dominant at room temperature, suggesting dislocation slip was the main deformation mechanism during the fatigue test. As AA6061-T6 (Al–Mg–Si) is a precipitation hardened alloy, the presence of various types of Mg and Si intermetallic particles such as β (Mg_2Si), β' (Mg_9Si_6), and semi-coherent β'' (Mg_5Si_6) has been recognised after ageing [9, 11, 15, 30–32]. Figure 11d shows an intermetallic precipitate, possibly β' with a diameter of ~ 10 nm, was sheared by a gliding dislocation.

Figure 12 shows the BF TEM images of the specimen after fatigue test at 108 K. Dislocation walls were also observed as shown in Fig. 12a. However, the dislocation walls after fatigue test at 108 K was narrower, and the dislocations forming the walls appeared less organised in comparison to that of the room temperature (Fig. 11a). Furthermore, the dislocation behaviour at 108 K was different to that of the room temperature; dislocation pinning became more noticeable with decreasing temperature as shown in Fig. 12b, c. Dislocations were pinned at the intermetallic precipitates, but in particular, dislocations appeared to pinned at β'' precipitates which are known to be sheared at room temperature [31, 32]. A high-resolution TEM (HR-TEM) image was taken at the point where a dislocation (indicated by dotted orange line) appeared to be pinned by a β'' precipitate (indicated by red dashed line) (Fig. 12d). The atom arrangement of the β'' precipitate was present without any distortion, suggesting the dislocation was not able to shear the precipitate at 108 K. Some of pinned dislocations exhibited bowing behaviour acting as a possible dislocation generation source during cyclic loading.

4 Discussion

4.1 Influence of Cryogenic Temperature on Tensile Behaviour

Results in Sect. 3.2 show that the monotonic tensile properties of the aluminium alloy 6061-T6 increased with decreasing temperatures (Fig. 3 and Table 2). The enhanced tensile properties of aluminium alloys at cryogenic temperatures have been recognised in many studies [4–13]. The enhanced yield stress was associated with increase in the Peierls stress with decreasing temperature [33, 34]. Dislocation movement involves breaking of bonding between atoms in a lattice, and the shear stress required to overcome the atomic bond strength to move dislocations is known as the Peierls stress. In general, atoms are
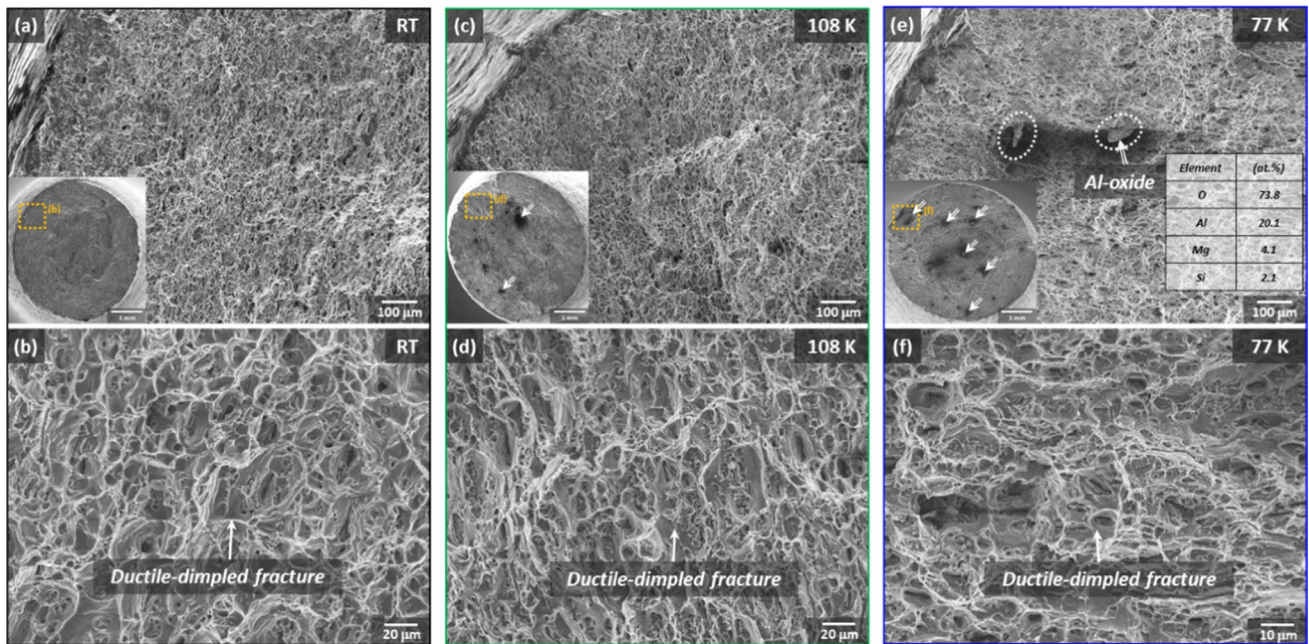
Fig. 6 Fracture surfaces of tensile tested specimens **a**, **b** at room temperature, **c**, **d** at 108 K, and **e**, **f** at 77 K. The white arrows shown in **c** and **e** indicate aluminium oxide inclusions on fracture surfaces of the specimens tested at 108 K and 77 K
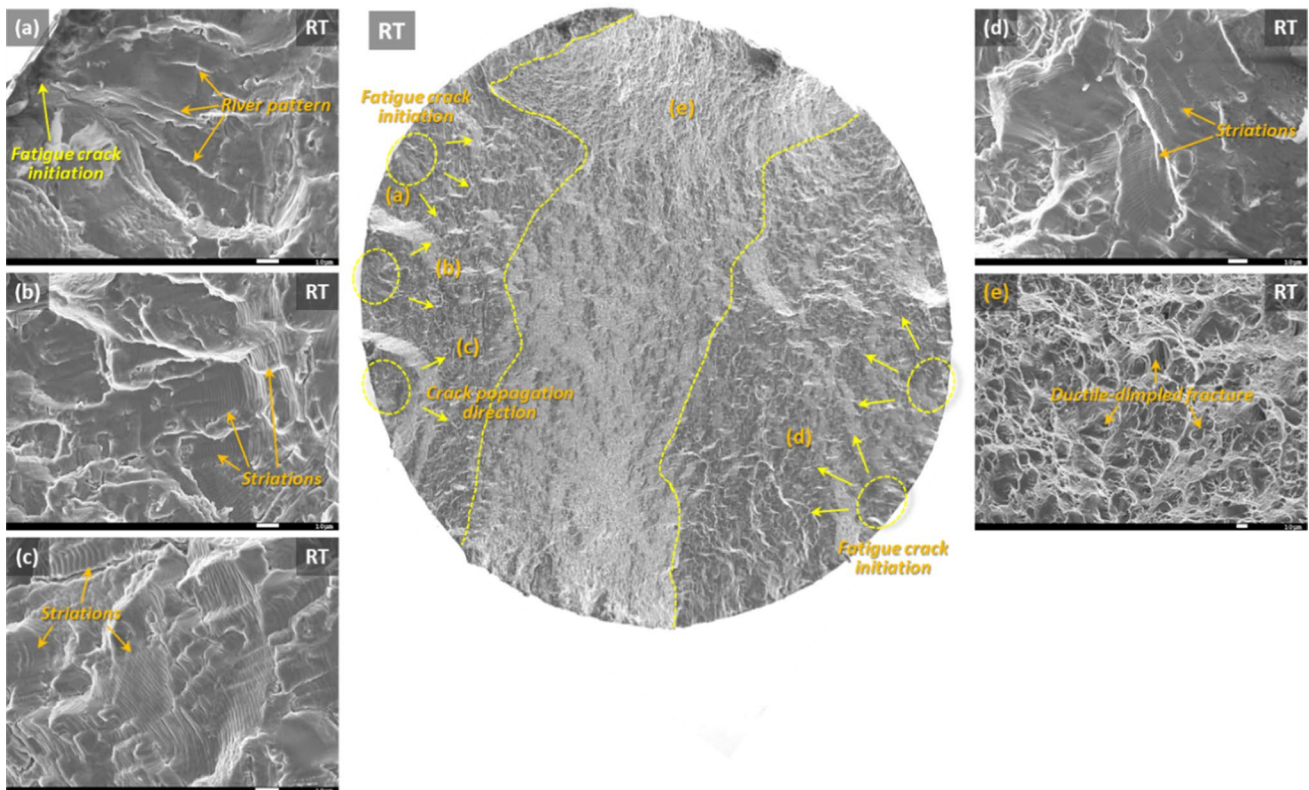

Fig. 7 SEM fractography of the sample tested at room temperature showing **a** crack initiation site with river patterns, **b**–**d** fatigue striations formed along crack propagation direction (towards the centre of cylindrical dog bone specimen), **d** ductile dimples at centre of the specimen
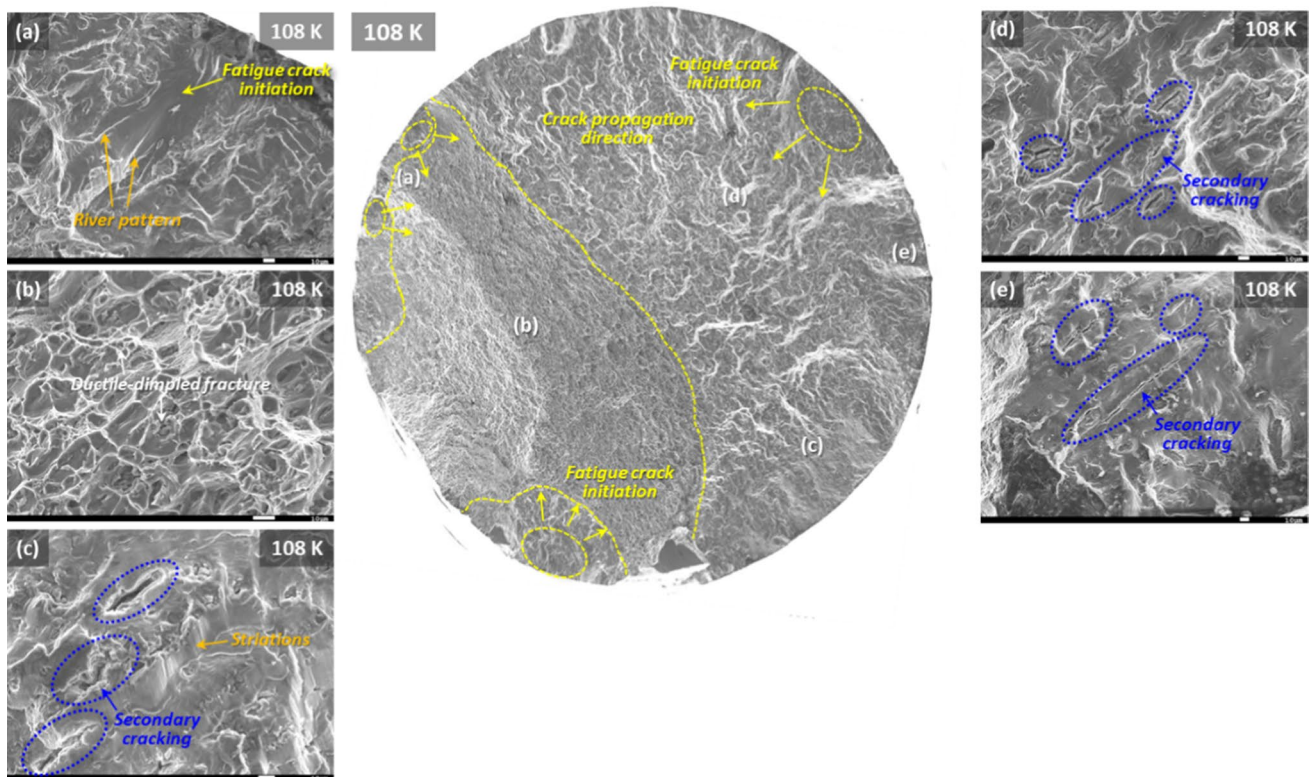
Fig. 8 SEM fractography of the sample tested at 108 K showing **a** crack initiation site with river patterns, **b** ductile dimples in overloaded region, **c–e** secondary cracking formed along the crack propagation direction indicated by blue ellipsoids

known to vibrate, and their vibration becomes more vigorous with increasing temperature thanks to thermal assistance. The thermal assistance results in a weaker atomic bond strength and hence the Peierls stress becomes lower at a higher temperature. On the other hand, the vibration of atoms diminishes at cryogenic temperatures due to a reduced thermal assistance. As a result, the increase in Peierls stress might have suppressed slip of mobile dislocations at lower temperatures, resulting in a higher stress required to start glide of dislocations [33].

The increased work hardening behaviour and uniform elongation at lower temperatures shown in Fig. 4 were due to suppressed dynamic recovery and subsequent high density of dislocations [7, 9–14, 35]. Dynamic recovery occurs via cross slip of screw dislocations and their annihilations [10, 36, 37]. The activation energy for cross slip is related to stacking fault energy. In general, stacking fault energy is known to decrease with decreasing temperature, and this leads to an increase in the activation energy [10, 36, 37]. Thus, the cross slip becomes less active (i.e., planar slip becomes dominant), and rate of the annihilation decreases at lower temperatures. Hence, a higher density of dislocations remained after plastic deformation at cryogenic temperatures as shown in Table 4. Gruber et al. [10] also confirmed presence of a high density of dislocations at

cryogenic temperature in Al–Mg alloy and Al–Mg–Si alloy after monotonic tensile tests using in-situ synchrotron. The dominant planar slip and increased dislocation density result in more frequent accumulations between planar dislocations, reducing dislocation mean free path. Therefore, a higher stress for dislocation glide is required to overcome the accumulated dislocation barrier due to the increased encounter frequency of the barrier. This increase in the critical stress for glide leads to a greater work hardening rate at cryogenic temperatures. The KAM distribution map (Fig. 9b) demonstrated the uniform distribution of dislocations according to the dislocation accumulation within the grain interior. This indicated the accommodation of homogeneous plastic deformation throughout the grain. The TEM observations by Xu et al.[5]. and Ma et al.[11]. also showed a high density of dislocations forming dislocation substructures with a uniform distribution within grain interior at cryogenic temperatures (113 K and 77 K). Furthermore, Xu et al. [5] and Cheng et al. [7] suggested the higher resistance to dislocation movement at cryogenic temperatures (the high Peierls stress and reduced dislocation mean free path) may reduce influence of the Schmid factor. Therefore, the slip along the favoured slip system became harder, the strain localisation at grain boundaries due to pile up of dislocation becomes less. Hence, the strain localisation was rather developed within
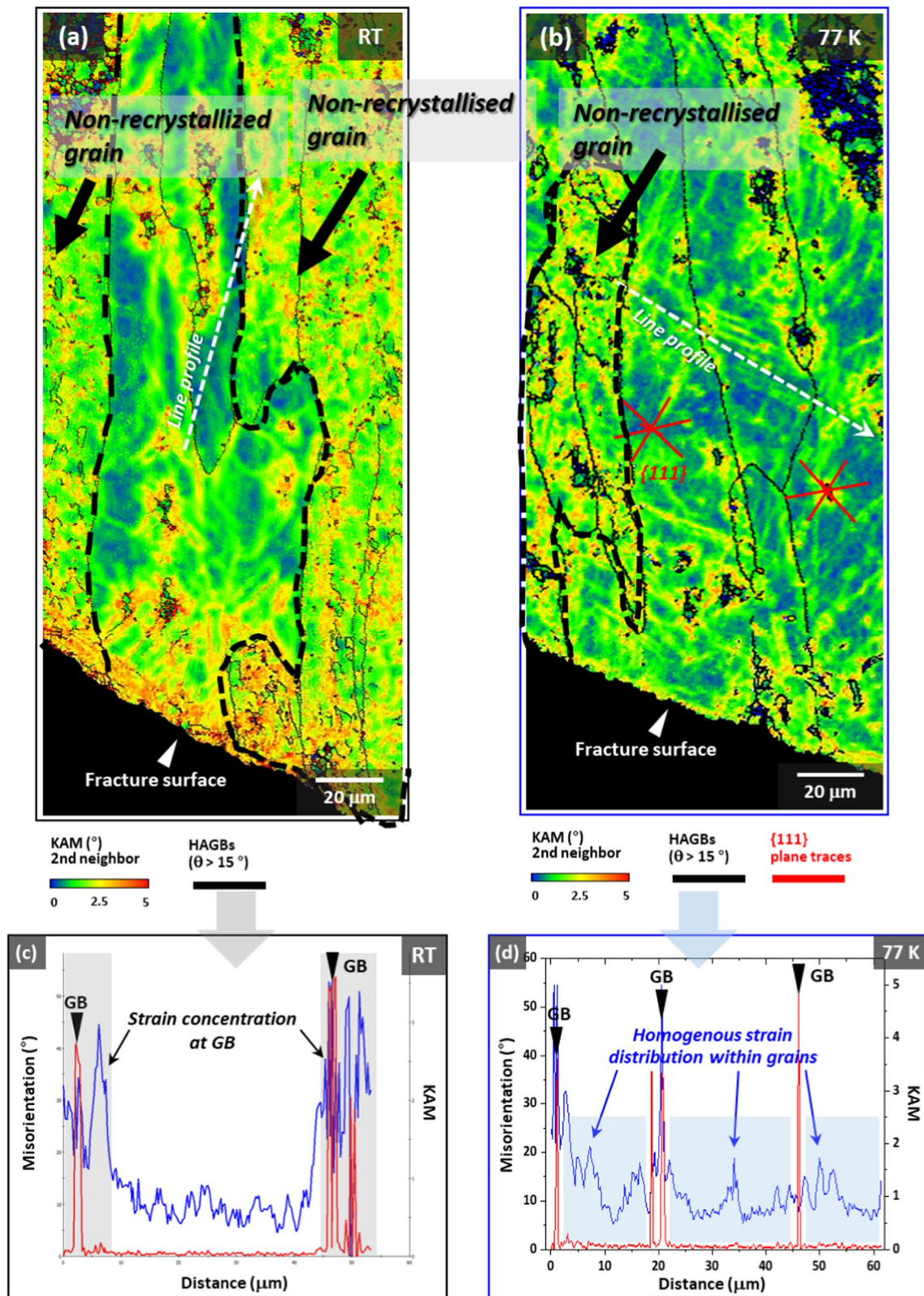
Fig. 9 **a**, **b** EBSD KAM maps of the specimens tested at room temperature and 77 K. **c**, **d** Misorientation and KAM values along line profile (the white dashed arrow line) in the KAM maps of the specimen tested at room temperature and 77 K, respectively
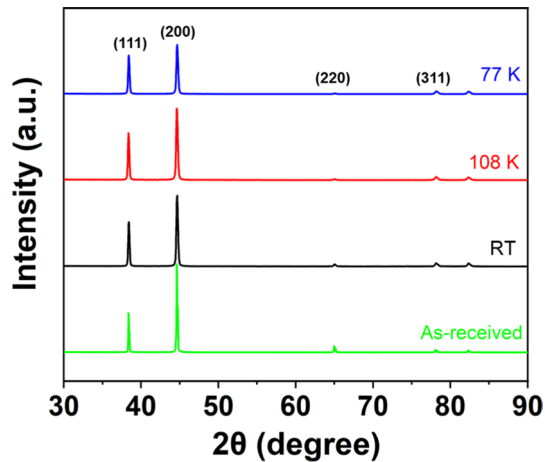
Fig. 10 X-ray diffraction patterns of AA6061-T6 with peaks corresponding to aluminium matrix in as-received state, and after tensile tests at room temperature (RT), 108 K and 77 K

the grain as shown in the KAM map (Fig. 9b). This strain localisation within the grain rather than the grain boundary also improves the uniform elongation at cryogenic temperatures.

4.2 Influence of Cryogenic Temperature on Fatigue Behaviour

In general, the initial dislocation density in the as-received state aluminium alloy 6061-T6 is low, but dislocation density increases significantly at the early stage of cyclic loading to accommodate the prescribed strain. The increase in dislocation density results in more interactions between dislocations, causing cyclic hardening and consequent increase in the maximum peak stress as shown in Fig. 5. Upon further cyclic loading, once dislocation density reaches its maximum, dislocations start to annihilate and rearrange to lower energy structures such as dislocation walls and cells [38–42]. This reduction in dislocation density resulted in cyclic softening. The BF-TEM images of the specimen fatigued at

room temperature demonstrates the presence of the dislocation walls formed during the cyclic softening stage (Fig. 11), whereas dislocation cells were not observed as the number of cycles was too short for the annihilation and rearrangement of dislocations.

However, the fatigue behaviour at 108 K is significantly different to that at room temperature. As described in Sect. 4.1, dislocation mobility was low due to the high Peierls stress and the dynamic recovery of screw dislocation via cross slip was suppressed at lower temperatures. Moreover, BF-TEM images (Figs. 11 and 12) showed dislocation slip was the single dominant deformation mechanism responsible for cyclic plasticity regardless of temperature. Therefore, the generation of mobile dislocations outweighed the annihilation of dislocations to accommodate prescribed strain, which in turn caused a longer cyclic hardening phase (up to the first 100th cycles). In contrast, the high mobility of dislocations thanks to the thermal assistance at room temperature means a smaller number of mobile dislocations was required to be generated to accommodate prescribed strain [43, 44]. Thus, a short cyclic hardening (up to first 5th cycles) was exhibited followed by the cyclic softening at room temperature. Interestingly, a constant maximum stress response up to ~ 700th cycle occurred after the cyclic hardening phase instead cyclic softening. The constant stress response could be the result of the change in dislocation slip behaviour; dislocations were pinned by β'' precipitate which can be sheared at room temperature (Fig. 12b–d) [11, 31, 32]. Such change in slip behaviour was associated with a greater shear modulus, the temperature dependent component of the Peierls stress, owing to the increased atomic bond strength at cryogenic temperature [45, 46]. The pinning effect by β'' precipitates contributed to an additional resistance to glide of dislocations, which resulted in a further reduction in the annihilation rate. Nevertheless, dislocations annihilated and rearranged into walls as shown in Fig. 12a, but with a narrower wall thickness in comparison to that at room temperature considering the restricted dislocation mobility. The constant maximum stress response phase suggests that

Table 4 Dislocation densities calculated based on XRD peak profiles using the Debye–Scherrer equation

| Specimen	Plane (hkl)	Degree (2θ)	FWHM (10^{-2} rad)	Dislocation density (10^{14} m^{-2})	(111) and (200) average dislocation density (10^{14} m^{-2})
As-received	111	38.39	0.279 ± 0.045	3.617 ± 0.96	4.256 ± 0.89
	200	44.65	0.332 ± 0.051	4.895 ± 1.22	
RT	111	38.4	0.367 ± 0.029	6.231 ± 0.82	7.698 ± 0.57
	200	44.66	0.454 ± 0.017	9.165 ± 0.57	
108 K	111	38.37	0.384 ± 0.008	6.840 ± 0.25	8.004 ± 0.29
	200	44.64	0.454 ± 0.014	9.166 ± 0.46	
77 K	111	38.4	0.384 ± 0.012	6.840 ± 0.36	8.361 ± 0.37
	200	44.67	0.471 ± 0.016	9.883 ± 0.54	
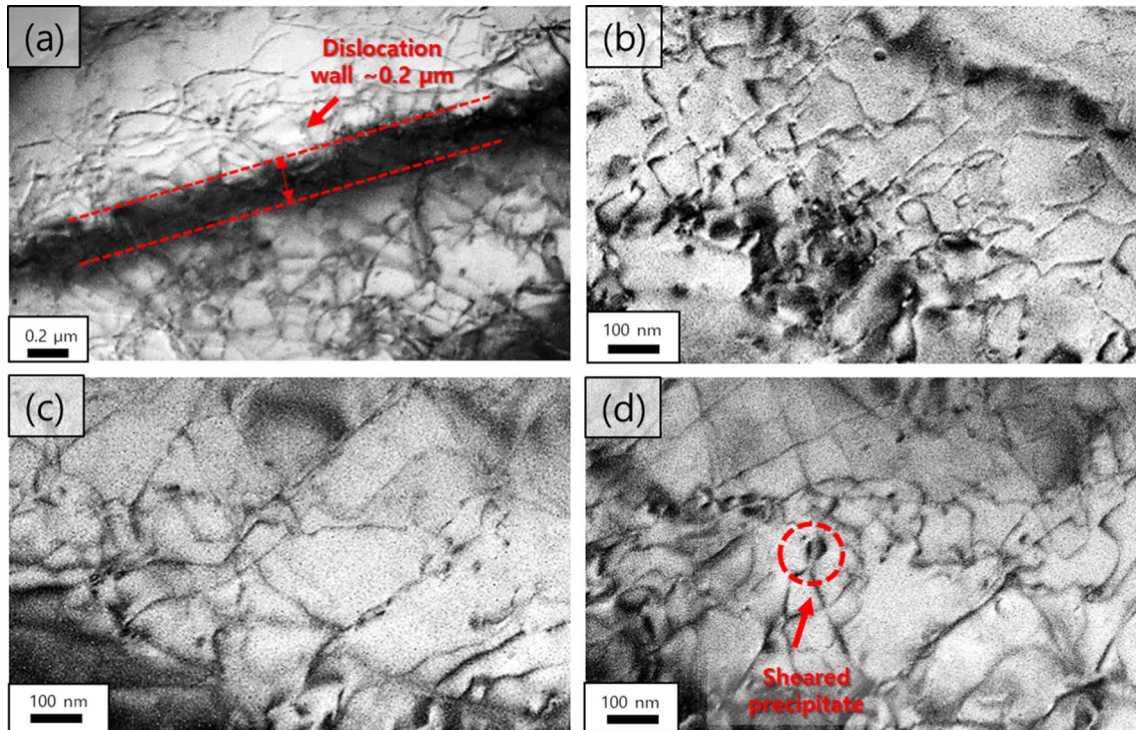
Fig. 11 **a–d** BF-TEM image of AA6061-T6 specimen after fatigue test at room temperature
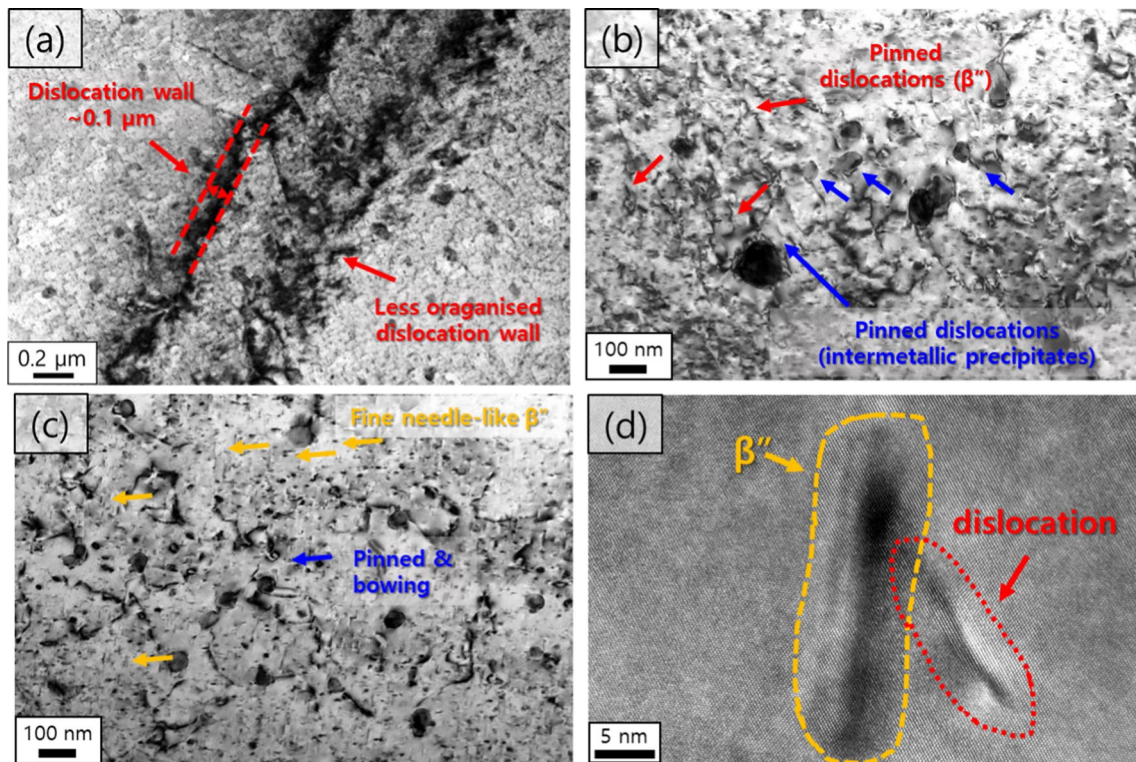

Fig. 12 **a–d** BF-TEM image of AA6061-T6 specimen after fatigue test at 108 K

an equilibrium between the dislocation generation and the annihilation could have been established.

As demonstrated in Fig. 5 and Table 3, the other significant influence of the cryogenic temperature was the improved fatigue life. Fractography showed the main cracks which led to a fatigue failure initiated from the free surface of the specimens fatigued at both temperature conditions (Figs. 7 and 8). In general, fatigue crack initiation is associated with the persistent slip band (PSBs) which consists of a large number of slip planes [17]. During cyclic loading, localised slip activity occurs along those PSBs and results in the discontinuity at the interface between matrix and PSBs. Such discontinuity leads to the formation of extrusions and intrusion, and subsequent roughening of free surface [47, 48]. Plastic strain localisation occurs at the rough free surface and crack initiation [38, 49–51]. However, the homogeneous deformation thanks to the evenly distributed dislocations at cryogenic temperature prohibited glide of dislocations along the favoured slip system and subsequent formation of slip bands as shown in Fig. 9e. Furthermore, fine β'' precipitates were dispersed evenly in comparison to other MgSi based intermetallic precipitates (Fig. 12b–d), contributing to the homogeneous deformation. As the formation of slip bands was suppressed, crack initiation was delayed at cryogenic temperatures, which in turn led to an improved fatigue life. The localised strain within grain interior could have acted as initiation sites for secondary cracks which propagated in the direction perpendicular to the primary cracks as shown in Fig. 8c–e. The initiation and propagation of secondary crack lowers stress intensity and absorbs the energy, retarding the growth of main cracks [52], contributing the enhanced fatigue life at 108 K.

5 Conclusion

The influence of cryogenic temperatures on the microstructure evolution and deformation behaviour of aluminium alloy 6061-T6 has been discussed in this study. The significant increase in yield stress of aluminium alloy 6061-T6 with decreasing temperature was associated with the stronger resistance to dislocation movement due to the reduced thermal assistance at cryogenic temperatures. Thus, a higher stress was required to overcome atomic bond strength and start glide of dislocations. Furthermore, the greater activation energy for the cross-slip of screw dislocations at lower temperatures suppressed dynamic recovery. As a result, a high density of dislocations was evenly distributed within grain interior and increased work hardening rate, which in turn resulted in homogeneous deformation behaviour and a higher ductility at cryogenic temperatures.

Dislocation slip was the main deformation mechanism during cyclic loading. At cryogenic temperature, a higher number of dislocations was generated to accommodate prescribed strain during cyclic loading as movement of dislocations were restricted. The generation of dislocations outweighed the annihilation of dislocations and resulted in the enhanced cyclic hardening behaviour. Cyclic softening behaviour was not observed at 108 K because of the low annihilation rate attributed to the pinning of dislocations by β'' precipitates. Fatigue life improved significantly at the cryogenic condition thanks to the homogeneous deformation which prohibited localised slip and delayed formation of persistent slip bands (PSBs) that act as crack initiation site. Fractography revealed the presence of the secondary cracks propagated in the direction perpendicular to main cracks on the fracture surface of the specimen fatigued 108 K. Their presence lowered stress intensity which resulted in the retardation of main crack growth and contributed to the improved fatigue life.

Authors contributions MJ: Conceptualization, Methodology, Investigation, Visualization, Validation, Formal analysis, Data curation, Writing – original draft. BL: Conceptualization, Methodology, Investigation, Visualization, Validation, Formal analysis, Data curation, Writing – review & editing. JY: Conceptualization, Methodology, Investigation, Visualization, Validation, Formal analysis, Data curation, Writing – review & editing. YJ: Investigation, Visualization, Validation, Formal analysis, Data curation, Writing – original draft. SL: Funding acquisition, Resources, Conceptualization, Methodology, Writing – review & editing, Supervision.

Declarations

References

1. S. McQueen, J. Stanford, S. Satyapal, E. Miller, N. Stetson, D. Papageorgopoulos, N. Rustagi, V. Arjona, J. Adams, K. Randolph, D. Peterson, L. Hill, M. Koleva, T. Reinhardt, E. Frye, R.

Schrecengost, A. Kokkinos, J. Litynski, R. Conrad, G. Solovei-chik, D. Tew, S. Litzelman, J. Vetrano, R. Onuschak, A. Hahn, E. Hsieh, R. Costa, *Department of Energy Hydrogen Program Plan* (U.S. Department of Energy, 2020). https://doi.org/10.2172/1721803

2. H. Li, R. Niu, W. Li, H. Lu, J. Cairney, Y.S. Chen, J. Nat. Gas Sci. Eng. **105**, 104709 (2022). https://doi.org/10.1016/j.jngse.2022.104709

3. A. Züttel, Sci. Nat. **91**, 157–172 (2004). https://doi.org/10.1007/s00114-004-0516-x

4. J. Glazer, S.L. Verzasconi, R.R. Sawtell, J.W. Morris, Metall. Trans. A **18**, 1695–1701 (1987). https://doi.org/10.1007/BF02646201

5. Z. Xu, H.J. Roven, Z. Jia, Mater. Sci. Eng. A **679**, 379–390 (2017). https://doi.org/10.1016/j.msea.2016.10.049

6. F. Dong, S. Huang, Y. Yi, B. Wang, H. He, Mater. Sci. Eng. A **809**, 140971 (2021). https://doi.org/10.1016/j.msea.2021.140971

7. W. Cheng, W. Liu, S. Yuan, Mater. Sci. Eng. A **759**, 357–367 (2019). https://doi.org/10.1016/j.msea.2019.05.047

8. D.H. Park, S.W. Choi, J.H. Kim, J.M. Lee, Cryogenics **68**, 44–58 (2015). https://doi.org/10.1016/j.cryogenics.2015.02.001

9. Y. Liu, X. Zhao, J. Li, L. Bhatta, K. Luo, C. Kong, H. Yu, J. Alloys Compd. **860**, 158449 (2021). https://doi.org/10.1016/j.jallcom.2020.158449

10. B. Gruber, I. Weißensteiner, T. Kremmer, F. Grabner, G. Falkinger, A. Schökel, F. Spieckermann, R. Schäublin, P.J. Uggowitzer, S. Pogatscher, Mater. Sci. Eng. A **795**, 139935 (2020). https://doi.org/10.1016/j.msea.2020.139935

11. Y. Ma, C. Liu, K. Miao, H. Wu, R. Li, X. Li, G. Fan, J. Alloys Compd. **947**, 169559 (2023). https://doi.org/10.1016/j.jallcom.2023.169559

12. F. Dong, Y. Yi, C. Huang, S. Huang, J. Alloys Compd. **827**, 154300 (2020). https://doi.org/10.1016/j.jallcom.2020.154300

13. D.Y. Park, M. Niewczas, Mater. Sci. Eng. A **491**, 88–102 (2008). https://doi.org/10.1016/j.msea.2008.01.065

14. L. Mei, X.P. Chen, G.J. Huang, Q. Liu, J. Alloys Compd. **777**, 259–263 (2019). https://doi.org/10.1016/j.jallcom.2018.11.012

15. C. Peng, G. Cao, T. Gu, C. Wang, Z. Wang, C. Sun, J. Mater. Res. Technol. **19**, 709–721 (2022). https://doi.org/10.1016/j.jmrt.2022.05.066

16. D.C.C. Magalhães, A.M. Kliauga, V.L. Sordi, Trans. Nonferrous Met. Soc. China **31**(6), 595–608 (2021). https://doi.org/10.1016/S1003-6326(21)65522-X

17. S. Suresh, Fatigue of Materials, 2nd edn. (Cambridge University Press, 1998), pp. 132–164. https://doi.org/10.1017/CBO9780511806575

18. W. Schütz, Eng. Fract. Mech. **54**, 263–300 (1996). https://doi.org/10.1016/0013-7944(95)00178-6

19. J. Schijve, Int. J. Fatigue **25**, 679–702 (2003). https://doi.org/10.1016/S0142-1123(03)00051-3

20. Y.B. Xu, L. Wang, Y. Zhang, Z.G. Wang, Q.Z. Hu, Metall. Trans. A **22**, 723–729 (1991). https://doi.org/10.1007/BF02670295

21. T. Yuri, T. Ogata, M. Saito, Y. Hirayama, Cryogenics **41**, 475–483 (2001). https://doi.org/10.1016/S0011-2275(01)00100-X

22. K.J. Park, C.S. Lee, Scripta Mater. **34**, 215–220 (1996). https://doi.org/10.1016/1359-6462(95)00505-6

23. K.T. Venkateswara Rao, R.O. Ritchie, Metall. Trans. A **22**, 191–202 (1991). https://doi.org/10.1007/BF03350961

24. G.E. Dieter, *Mechanical Metallurgy*, SI Metric edn. (McGraw-Hill Book Company, London, 1988)

25. N. Choi, K.R. Lim, Y.S. Na, U. Glatzel, J.H. Park, J. Alloys Compd. **763**, 546–557 (2018). https://doi.org/10.1016/j.jallcom.2018.05.339

26. J.P. Hirth, in *Physical Metallurgy*, ed. By R.W. Cahn, P. Haasen (Elsevier, North Holland, 1996), pp. 1831–1875. https://doi.org/10.1016/B978-044489875-3/50025-9

27. G. Yergaliuly, B. Soltabayev, S. Kalybekkyzy, Z. Bakenov, A. Mentbayeva, Sci. Rep. **12**, 851 (2022). https://doi.org/10.1038/s41598-022-04782-2

28. Y.S. Eom, J.M. Park, J.W. Choi, D.J. Seong, H. Joo, Y.C. Jo, K.T. Kim, J.H. Yu, I. Son, J. Alloys Compd. **956**, 170348 (2023). https://doi.org/10.1016/j.jallcom.2023.170348

29. Z.Y. Zhong, H.G. Brokmeier, W.M. Gan, E. Maawad, B. Schwebke, N. Schell, Mater. Charact. **108**, 124–131 (2015). https://doi.org/10.1016/j.matchar.2015.09.004

30. A.P. Sekhar, A.B. Mandal, D. Das, J. Mater. Res. Technol. **9**, 1005–1024 (2020). https://doi.org/10.1016/j.jmrt.2019.11.040

31. K. Misumi, K. Kaneko, T. Nishiyama, T. Maeda, K. Yamada, K.I. Ikeda, M. Kikuchi, K. Takata, M. Saga, K. Ushioda, J. Alloys Compd. **600**, 29–33 (2014). https://doi.org/10.1016/j.jallcom.2014.02.059

32. Y. Wang, Y. Lu, S. Zhang, H. Zhang, H. Wang, Z. Chen, J. Alloys Compd. **885**, 161028 (2021). https://doi.org/10.1016/j.jallcom.2021.161028

33. D.C. Yang, Y.H. Jo, Y. Ikeda, F. Körmann, S.S. Sohn, J. Mater. Sci. Technol. **90**, 159–167 (2021). https://doi.org/10.1016/j.jmst.2021.02.034

34. D. Caillard, J.L. Martin, Pergamon. Mater. Ser. **8**, 227–277 (2003). https://doi.org/10.1016/S1470-1804(03)80037-8

35. Z. Xu, H.J. Roven, Z. Jia, Mater. Sci. Eng. A **648**, 350–358 (2015). https://doi.org/10.1016/j.msea.2015.09.083

36. L. Rémy, A. Pineau, B. Thomas, Mater. Sci. Eng. **36**(1), 47–63 (1978). https://doi.org/10.1016/0025-5416(78)90194-5

37. P. Feltham, Philos. Mag. **6**(72), 1479–1486 (1961). https://doi.org/10.1080/00318086.1961.11643277

38. D. Kuhlmann-Wilsdorf, C. Laird, Mater. Sci. Eng. **27**(2), 137–156 (1977). https://doi.org/10.1016/0025-5416(77)90166-5

39. H. Mughrabi, Acta Metall. **31**(9), 1367–1379 (1983). https://doi.org/10.1016/0001-6160(83)90007-X

40. H. Mughrabi, Mater. Sci. Eng. **33**(2), 207–223 (1978). https://doi.org/10.1016/0025-5416(78)90174-X

41. M.S. Pham, S.R. Holdsworth, Procedia Eng. **10**, 1069–1074 (2011). https://doi.org/10.1016/j.proeng.2011.04.176

42. D. Kuhlmann-Wilsdorf, C. Laird, Mater. Sci. Eng. **46**(2), 209–219 (1980). https://doi.org/10.1016/0025-5416(80)90176-7

43. M. Jin, E. Hosseini, S.R. Holdsworth, M. Pham, Addit. Manuf. **51**, 102600 (2022). https://doi.org/10.1016/j.addma.2022.102600

44. B. Devincre, L.P. Kubin, Mater. Sci. Eng. A **234–236**, 8–14 (1997). https://doi.org/10.1016/s0921-5093(97)00146-9

45. X. Zhang, W. Li, Y. Li, J. Ma, Y. Deng, J. Shao, X. Wu, Intermetallics **91**, 86–89 (2017). https://doi.org/10.1016/j.intermet.2017.08.013

46. R. Farraro, R.B. McLellan, Metall. Trans. A **8**, 1563–1565 (1977). https://doi.org/10.1007/BF02644859

47. J.A. Ewing, J.C.W. Humfrey, Philos. Trans. R. Soc. A **200**, 321–330 (1903). https://doi.org/10.1098/rsta.1903.0006

48. D. Hull, D.J. Bacon, in *Introduction to Dislocations*, 5th edn. (Butterworth-Heinenmann, Oxford, 2011), pp. 43–62. https://doi.org/10.1016/C2009-0-64358-0

49. N. Thompson, N. Wadsworth, N. Louat, Philos. Mag. **1**(2), 113–126 (1956). https://doi.org/10.1080/14786435608238086

50. R. Wang, H. Mughrabi, S. McGovern, M. Rapp, Mater. Sci. Eng. **65**(2), 219–233 (1984). https://doi.org/10.1016/0025-5416(84)90084-3

51. H. Mughrabi, Philos. Trans. R. Soc. A **373**, 2038 (2015). https://doi.org/10.1098/rsta.2014.0132

52. A. Das, H.W. Viehrig, E. Altstadt, F. Bergner, J. Hoffmann, Crystals **8**(8), 306 (2018). https://doi.org/10.3390/cryst8080306

Publisher's Note Springer Nature remains neutral with regard to jurisdictional claims in published maps and institutional affiliations.